JOURNAL OF COMPUTATIONAL PHYSICS 15, 320–344 (1974)

A Study of Convective Heat Transfer in a Supersonic Recirculating Flow Region by Telenin's Method*

JAMES C. S. MENG†

NAS–NRC Postdoctoral Associate at George C. Marshall Space Flight Center, Alabama 35812

Received December 31, 1973; revised March 15, 1974

A theoretical analysis of the laminar base flow field of a two-dimensional reentry body has been formulated using Telenin's method. The numerical method divides the flow domain into horizontal strips along the x-axis and represents the flow variables as Lagrange interpolation polynomials in the vertical coordinate. The complete Navier-Stokes equations are used in the near wake region, and the boundary layer equations are applied elsewhere. The boundary conditions consist of the flat plate thermal boundary layer in the forebody region and the near wake profile in the downstream region. The resulting two-point boundary value problem of 33 ordinary differential equations is then solved by the multiple shooting method using 12 segments.

The theoretical aspects of the convergence of the present scheme are discussed thoroughly and are compared to the successful convergence of a smaller system; i.e. the two-dimensional, two-phase stagnation point flow solution. The unsatisfactory convergence of the present study, which is attributed to two shortcomings in the formulation, can be improved if the following two steps are taken. First, a variable transformed coordinate should be incorporated to allow different stretching in various segments such that the instabilities encountered can be avoided. Secondly, the Lagrange interpolation polynomials should be replaced by other forms of polynomials or analytic functions to remove the mathematical singularity at the rear stagnation point.

The specific case considered in this report is that of vehicle reentry at zero angle of attack in a Mach 11 free stream with Reynolds number $Re_{\infty,H}$ ranging from 0.8×10^5 to 1.2×10^5. The base wall temperature remains constant at 255°K (460° R) and the free stream temperature is 217.43° K (392.28° R). It was assumed that heat conductivity and viscosity are linearly proportional to temperature, the specific heat is constant, and the Prandtl number is unity. The detailed flow field and thermal environment in the base region are presented in the form of temperature contours, Mach number contours, velocity vectors, pressure distributions, and heat transfer coefficients on the base surface. The maximum heating rate was found to be always on the centerline, and the two-dimensional stagnation point flow solution was adequate to estimate this value as long as the local Reynolds number could be obtained.

* Presented at the Third International Conference on Numerical Methods in Fluid Dynamics in 1971.

† Present address: Physical Dynamics, Inc., P. O. Box 1069, Berkeley, Ca. 94701.

Copyright © 1974 by Academic Press, Inc.
All rights of reproduction in any form reserved.

INTRODUCTION

With the introduction of reusable space vehicles, such as the Space Shuttle, minimum weight and reusability have become more important factors. To design the base region thermal protection system so that an undue weight penalty is not assessed to the vehicle, an accurate prediction of the reentry base region thermal environment is required. In addition, an accurate definition of the reentry base environment is required because the main engine nozzles are situated in the base region and are exposed to trapped recirculating gases during reentry. The purpose of this study is to provide a better understanding of the base separated flow region during reentry so that a more accurate reentry base thermal environment can be obtained.

Atmospheric reentry involves total temperature and Mach number conditions that cannot be effectively simulated experimentally. Numerical schemes which can yield accurate solutions without requiring large storage capacity and long execution time for computers are desirable. One such scheme established by Telenin and Tinyakov [1] exploits the obvious numerical advantages of working with Cauchy-type problems for the present elliptic system of equations. It was first proposed for axisymmetric blunt body problems and later adopted for conical flow problems by Holt and Ndefo [2]. It is well known that Cauchy's problems are in general improperly posed for an elliptic system of equations. However, for an *a priori* restricted class of solutions (such as the class of bounded analytic functions), Cauchy's problems become correctly posed for the elliptic systems. Mathematically, this means that to solve an elliptic system of equations by hyperbolic means would necessarily introduce the limitation that the solution can only be obtained in certain classes of functions, and the solution for this hyperbolic system exists only when the flow domain does not contain any discontinuities. Since the new hyperbolic system is arbitrary, in other words no characteristics exist, the integration of equations can be performed in any direction. Physically this is the process that allows the disturbances to propagate over the entire flow domain.

Assume that the base region is composed of the base wall and two protruding shrouds (Fig. 1). The cavity walls, the free mixing layer, and the near wake region define the bounded domain wherein Telenin's scheme applies. The Navier-Stokes and boundary layer equations are transformed so that the region of interest becomes a rectangle that is subsequently divided into strips along the shrouds; Lagrange interpolation polynomials of degree four and seven are applied in the cavity and the near wake region across the strips. Augmented first-order ordinary differential equations are obtained. The problem is then reduced to a two-point boundary value problem.

Errors committed in the arbitrary trial data increase exponentially with the number of trial variables and the physical dimension of the integration domain, so

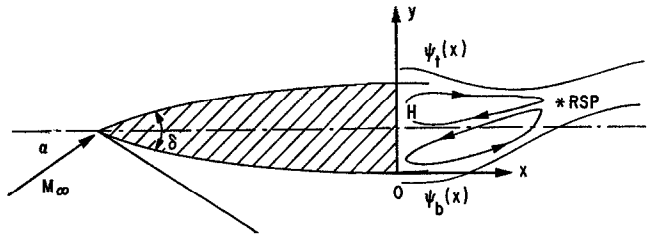

FIG. 1. Physical sketch of a two-dimensional Space Shuttle base region.

Telenin's scheme is not immune to instability. This is especially true in the present case, because an almost singular layer, i.e. the base wall thermal boundary layer, exists right at the initial point. Because of the high flow variable gradients there, the errors introduced by inaccurate guessing of the initial values are amplified so rapidly that integration cannot be carried through this region. Such instability, which often appears in dealing with nonlinear problems, is the major difficulty in applying Telenin's scheme. To handle this problem, the common simple shooting method is inadequate. The parallel or multiple shooting method proposed by Morrison *et. al.* [3] and later developed by Bulirsch [4] is found effective in overcoming the instability. In essence, the multiple shooting method reduces the integration domain length by subdividng the flow domain into a number of segments; each segment is treated by the simple shooting method. The guessed initial values are corrected iteratively by solving a linear system to satisfy the overall boundary conditions on both ends and to eliminate the discontinuities occurring at the segment junction points.

There are several important advantages of the present scheme over a finite-difference type computation. It occupies one or two orders of magnitude smaller storage space; it consumes at least two orders of magnitude less computer time per iteration; the analyticity of the solution is guaranteed; and the equations are satisfied exactly on the strips. A simple estimate is given to support these assertions. The storage required for the present scheme is only that for storing variables at the intersection points of the strips and the segments; it is one or two orders of magnitude smaller than the number of grid points for the finite-difference scheme. The computation time for the present scheme is needed for the following three types of operations:

1. Integration of N (number of variables) $\cdot$ S (number of strips) $\cdot$ M (number of segments) equation.
2. Integration of $M \cdot (N \cdot S)^2$ variational equations.
3. Inversion of $MN \cdot S$ by $N \cdot S$ matrices.

The number of operations for one iteration is then approximately $MN^3S^3 + M(NS + N^2S^2)F$ (number of integration step) or $\cong 10^6$ with $M = 12$, $N = 7$,

$S = 7$, and $F = 10$. The total computation time per iteration is about 1 sec while a finite-difference scheme would have to invert an $MNSF$ by $MNSF$ matrix or about $MN^3S^3F^3$ operations or 10^3 sec per iteration.

Formulation of the Problem

As shown in Fig. 1, the origin is set at the bottom corner of the base wall and the region of interest is surrounded by the base wall, the boundary layers on both shrouds, and the near wake region. The basic equations are the continuity equation, the Navier-Stokes equations, and the energy equation.

$$\frac{\partial}{\partial x}(\rho u) + \frac{\partial}{\partial y}(\rho v) = 0. \tag{1}$$

$$\rho u \frac{\partial u}{\partial x} + \rho v \frac{\partial u}{\partial y} = -\frac{\partial p}{\partial x} + \frac{\partial}{\partial x}\left[\mu\left(2\frac{\partial u}{\partial x} - \frac{2}{3}\nabla \cdot \mathbf{u}\right)\right] + \frac{\partial}{\partial y}\left[\mu\left(\frac{\partial u}{\partial y} + \frac{\partial v}{\partial x}\right)\right]. \tag{2}$$

$$\rho u \frac{\partial v}{\partial x} + \rho v \frac{\partial v}{\partial y} = -\frac{\partial p}{\partial y} + \frac{\partial}{\partial y}\left[\mu\left(2\frac{\partial v}{\partial y} - \frac{2}{3}\nabla \cdot \mathbf{u}\right)\right] + \frac{\partial}{\partial x}\left[\mu\left(\frac{\partial u}{\partial y} + \frac{\partial v}{\partial x}\right)\right]. \tag{3}$$

$$C_v\left(\rho u \frac{\partial T}{\partial x} + \rho v \frac{\partial T}{\partial y}\right) = u\frac{\partial p}{\partial x} + v\frac{\partial p}{\partial y} + \frac{\partial}{\partial x}\left(k\frac{\partial T}{\partial x}\right) + \frac{\partial}{\partial y}\left(k\frac{\partial T}{\partial y}\right) + \mu\left\{2\left[\left(\frac{\partial u}{\partial x}\right)^2 + \left(\frac{\partial v}{\partial y}\right)^2\right] + \left(\frac{\partial v}{\partial x} + \frac{\partial u}{\partial y}\right)^2 - \frac{2}{3}(\nabla \cdot \mathbf{u})^2\right\}. \tag{4}$$

$$p = \rho RT. \tag{5}$$

Nondimensionalize all flow variables by their corresponding free stream values, and pressure is made dimensionless by $\rho_\infty U_\infty^2$. We assume that the gas is ideal, the specific heat is constant, the Prandtl number is unity, and the viscosity and heat conductivity are linearly proportional to the temperature. Transforming the region of interest from the physical plane to the ξ, η plane which is defined by

$$\xi = \frac{x}{H}$$

$$\eta = \frac{y - \Psi_b(x)}{\Psi_t(x) - \Psi_b(x)},$$

where $\Psi_t(x)$ and $\Psi_b(x)$ are top and bottom boundary layer edges, the region of interest becomes a rectangle bounded by $\eta = 0$, $\eta = 1$, $\xi = 0$ and the near wake boundary (Fig. 2). Replacing the first order derivatives by

$$\begin{pmatrix} \epsilon \\ \sigma \\ \beta \end{pmatrix} = H \frac{\partial}{\partial x} \begin{pmatrix} u \\ v \\ T \end{pmatrix},$$

substituting these into equations (1) through (4), carrying out the transformation according to

$$\frac{\partial}{\partial x} = \frac{1}{H\zeta}\left[\zeta \frac{\partial}{\partial \xi} - (\dot{\tau} + \eta\dot{\zeta}) \frac{\partial}{\partial \eta}\right]$$

$$\frac{\partial}{\partial y} = \frac{1}{H\zeta} \frac{\partial}{\partial \eta}, \qquad \text{and} \quad \zeta = \frac{\Psi_t(x) - \Psi_b(x)}{H}$$

and rearranging, we obtain:

$$\zeta u \rho_\xi = (\dot{\tau} + \eta\dot{\zeta})\, u\rho_\eta - \rho\epsilon\zeta - \rho_\eta v - \rho v_\eta, \tag{6}$$

$$\begin{aligned} \frac{4}{3}\frac{T\zeta^2}{Re}\epsilon_\xi = &-(\dot{\tau} + \eta\dot{\zeta})\left(\frac{\zeta T}{\gamma M_\infty^2}\rho_\eta - \frac{4}{3}\frac{\zeta T}{Re}\epsilon_\eta\right) + \frac{\zeta^2 T}{\gamma M_\infty^2}\rho_\xi \\ &+ \rho u\epsilon\zeta^2 + \rho v u_\eta \zeta + \frac{1}{\gamma M_\infty^2}\rho\beta\zeta^2 \\ &- \frac{1}{Re}\left[\frac{2}{3}\zeta\beta(2\epsilon\zeta - v_\eta) + T_\eta(u_\eta + \sigma\zeta) + T\left(u_{\eta\eta} + \frac{1}{3}\sigma_\eta\zeta\right)\right], \end{aligned} \tag{7}$$

$$\begin{aligned} \frac{T\zeta^2}{Re}\sigma_\xi = &(\dot{\tau} + \eta\dot{\zeta})\frac{\zeta T}{Re}\sigma_\eta + \rho u\sigma\zeta^2 + \rho v v_\eta \zeta + \frac{\zeta}{\gamma M_\infty^2}(\rho_\eta T + \rho T_\eta) \\ &- \frac{2}{3Re}[T_\eta(2v_\eta - \epsilon\zeta) + T(2v_{\eta\eta} - \zeta\epsilon_\eta)] \\ &- \frac{1}{Re}[\beta(u_\eta\zeta + \sigma\zeta^2) + T\epsilon_\eta\zeta], \end{aligned} \tag{8}$$

$$\begin{aligned} \frac{T\zeta^2}{Re\,Pr}\beta_\xi = &(\dot{\tau} + \eta\dot{\zeta})\left(\frac{\gamma - 1}{\gamma} u T\zeta\rho_\eta + \frac{1}{Re\,Pr}\zeta T\beta_\eta\right) \\ &- \frac{\gamma - 1}{\gamma} u T\zeta^2\rho_\xi + \rho u\beta\zeta^2 + \rho v\zeta T_\eta - \frac{\gamma - 1}{\gamma}(\rho u\beta\zeta^2 + vT\zeta\rho_\eta + \rho v\zeta T_\eta) \\ &- \frac{1}{Re\,Pr}\beta^2\zeta^2 - \frac{1}{Re\,Pr}(TT_\eta)_\eta \\ &+ \frac{(\gamma - 1)M_\infty^2}{Re} T\left[\frac{4}{3}(\epsilon^2\zeta^2 + v_\eta^2 - \epsilon\zeta v_\eta) + (\sigma\zeta + u_\eta)^2\right], \end{aligned} \tag{9}$$

$$\zeta u_\xi = (\dot{\tau} + \eta\dot{\zeta})\, u_\eta + \epsilon\zeta, \tag{10}$$

$$\zeta v_\xi = (\dot{\tau} + \eta\dot{\zeta})\, V_\eta + \sigma\zeta, \tag{11}$$

$$\zeta T_\xi = (\dot{\tau} + \eta\dot{\zeta})\, T_\eta + \beta\zeta, \tag{12}$$

$$\dot{\tau} = \frac{d}{d\xi}\frac{\Psi_b(x)}{H} = \tan\,[\nu(M_b) - \nu(M_{bo})], \tag{13}$$

$$\dot{\zeta} = \frac{d}{d\xi}\frac{\Psi_t(x) - \Psi_b(x)}{H} = \tan\,[\nu(M_{to}) - \nu(M_t)] - \dot{\tau}, \tag{14}$$

where subscripts ξ and η denote $d/d\xi$ and $\partial/\partial\eta$. $\nu(M)$ is the Prandtl–Meyer function. The subscripts b and bo indicate bottom boundary layer edge conditions at arbitrary ξ and at $\xi = 0$; similar conditions on the top boundary are denoted by t and to. We shall divide the domain of interest into S-1 strips, as shown in Fig. 2,

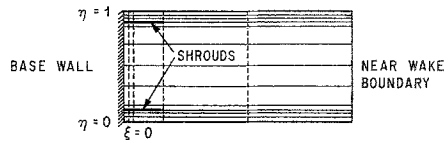

FIG. 2. Construction of strips and segments on transformed plane.

and approximate the flow variables in terms of Lagrange interpolation polynomials across the strips; i.e.

$$\begin{bmatrix} u(\xi,\eta) \\ v(\xi,\eta) \\ \rho(\xi,\eta) \\ T(\xi,\eta) \\ \epsilon(\xi,\eta) \\ \sigma(\xi,\eta) \\ \beta(\xi,\eta) \end{bmatrix} \cong \sum_{i=1}^{S} \begin{bmatrix} u_i(\xi) \\ v_i(\xi) \\ \rho_i(\xi) \\ T_i(\xi) \\ \epsilon_i(\xi) \\ \sigma_i(\xi) \\ \beta_i(\xi) \end{bmatrix} \prod_{\substack{k=1 \\ k\neq i}}^{S} \frac{(\eta - \eta_k)}{(\eta_i - \eta_k)}. \tag{15}$$

These expressions are substituted into Eqs. (6)–(12) with the requirement that the resulting equations be satisfied identically on each line η_i. An approximating system of $7S$ first-order ordinary differential equations is then obtained for the approximate values u_i, v_i, ρ_i, T_i, ϵ_i, σ_i, and β_i of the dependent variables on the S lines; η_i = constant. For the present case $S = 7$ and the η_i's are 1, 0.95, 0.90, 0.85, 0.73333, 0.61667, and 0.5.

Error Growth in the Boundary Layer

The major difficulty encountered in carrying out the present computation was the instabilities. Gilinskiy and Telenin [5] showed that an error caused by the approximation of flow variables by Lagrange interpolation polynomials across the strips may oscillate along the strips in the linear case. In present nonlinear systems, the error not only oscillates but grows rapidly to the neighboring strips. To cope with this, the author relied upon two fundamental tools, the boundary layer equations and the multiple shooting method; the latter will be discussed in the next section.

The entire flow domain of interest was first conceived to be governed by the Navier–Stokes Eqs. (1) through (5) so that the problem could be treated through a unified point of view. However this treatment experienced tremendous problems of instability because the uniform validity of the Navier-Stokes equations practically breaks down when dealing with a problem of extremely nonuniform grids. For high Reynolds number flows with a large separation bubble, the boundary layer equations are more feasible for the high gradient areas. Although this limit the accuracy of the solution to less than $1/Re$ there, the instability problem can be avoided partially.

The problem of error propagation in the base wall boundary layer is of special importance because almost all the physical processes in determining the base flow heat transfer properties occur there and in the free shear layers. The governing equations for flow can also be regarded as the error propagation equations, since without knowing the solution *a priori* the guessed initial values may contain an error of their own magnitude. We shall focus our attention upon the error growth of the heating rate across the base wall boundary layer. The following equation gives the growth rate of $\beta = H\partial T/\partial x$ at $\xi = 0$ along the strip:

$$\beta_\xi = \frac{1}{\zeta}(\dot{\tau} + \eta\dot{\zeta})\,\beta_\eta - \beta^2 - (\gamma - 1)\,M_\infty^2 PrT\sigma^2 + RePrF(\rho, T, \epsilon, \sigma, \beta). \tag{16}$$

The last term on the right side can be neglected if boundary layer equations are used; however, if it is retained on the Navier–Stokes equations, rapid error amplification caused by this term will occur since the initial values cannot always be chosen so as to guarantee the last term's smallness. The second and third terms are dominant then and remain to be negative; this will therefore reduce the danger of divergence. The approximate solution of the above equation can be represented by the following relation:

$$\frac{2}{\beta} - \frac{1}{((\gamma - 1)\,M_\infty^2 PrT\sigma^2)^{1/2}} \tan^{-1} \frac{\beta}{((\gamma - 1)\,M_\infty^2 PrT\sigma^2)^{1/2}} \cong \xi, \tag{17}$$

so that β will decrease when ξ increases; in other words the integration is stable. Similar analyses can also establish the fact that in shear layers the error is amplified slower by boundary layer equations than by Navier–Stokes equations. Based upon this result, we shall use boundary layer equations on base wall, shrouds, and in free shear layers and Navier-Stokes equations in the remaining regions. This mathematical model is depicted in Fig. 3.

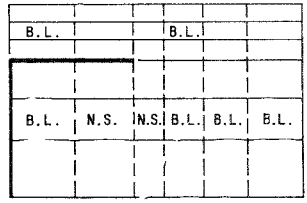

FIG. 3. Governing equations and segmentation of the base flow regions.

Boundary Layer Equations

In the base wall thermal boundary layer, Eqs. (11) and (12) are supplemented by the following governing equations:

$$\zeta\rho_\xi = (\dot{\tau} + \eta\dot{\zeta})\,\rho_\eta - \frac{1}{T}\,\rho\beta\zeta, \tag{18}$$

$$\frac{4}{3}\,T\zeta\epsilon_\xi = \frac{4}{3}\,T(\dot{\tau} + \eta\dot{\zeta})\,\epsilon_\eta + Re(\rho u\epsilon\zeta + \rho v u_\eta) - \frac{2}{3}\,\beta(2\epsilon\zeta - v_\eta) - \sigma T_\eta - \frac{1}{3}\,T\sigma_\eta\,, \tag{19}$$

$$\frac{T\zeta^2}{Re}\,\sigma_\xi = (\dot{\tau} + \eta\dot{\zeta})\,\frac{T}{Re}\,\sigma_\eta + \rho u\sigma\zeta^2 + \rho v v_\eta\zeta + \frac{\zeta}{\gamma M_\infty^2}\,(\rho_\eta T + \rho T_\eta) - \frac{\beta\sigma\zeta^2}{Re}\,, \tag{20}$$

$$\frac{\zeta}{Re\,Pr}\,\beta_\xi = (\dot{\tau} + \eta\dot{\zeta})\,\frac{1}{Re\,Pr}\,\beta_\eta + \rho u\beta\zeta + \rho v T_\eta - \frac{\gamma - 1}{\gamma}\,v(\rho T)_\eta - \frac{\zeta}{Re\,Pr}\,\beta^2 - \frac{(\gamma - 1)\,M_\infty^2}{Re}\,T\sigma^2\zeta, \tag{21}$$

$$\rho u\zeta u_\xi = (\dot{\tau} + \eta\dot{\zeta})(\rho u_\eta + \rho_\eta u) - u\zeta\rho_\xi - (\rho_\eta v + \rho v_\eta). \tag{22}$$

In the forebody thermal boundary layer and shear layer downstream of the shrouds the following set of equations is applied:

$$\rho u\zeta^2 u_\xi = \rho u\zeta(\dot{\tau} + \eta\dot{\zeta})\, u_\eta - \rho v u_\eta \zeta + \rho_1 u_1 \zeta^2 u_{1\xi} + \frac{1}{Re}(T_\eta u_\eta + T u_{\eta\eta}), \tag{23}$$

$$\rho u\zeta^2 T_\xi = \rho u\zeta(\dot{\tau} + \eta\dot{\zeta})\, T_\eta - \rho v T_\eta \zeta - (\gamma - 1)\, M_\infty^2 u\zeta^2 \rho_1 u_1 u_{1\xi} + \frac{1}{Re\, Pr}(TT_\eta)_\eta + \frac{(\gamma - 1)\, M_\infty^2}{Re} T(u_\eta)^2, \tag{24}$$

$$\rho T = \rho_1 T_1, \tag{25}$$

$$\epsilon_\xi, \sigma_\xi, \beta_\xi = 0. \tag{26}$$

Substituting relation (15) into Eqs. (18)–(22) and Eqs. (23)–(26), we obtain an approximating system of 7×4 first order ordinary differential equations for the base wall thermal boundary layer, 7×4 equations for the forebody boundary layer, and $7S$ equations for the shear layer. Along the strip $\eta = \eta_4$ in segment 3, where the Navier–Stokes equations are applied on and below it and the boundary layer equations are applied above it, the vertical derivatives are calculated by using the same seventh order Lagrange interpolation polynomials so that the vertical derivatives are continuous across this strip. In the first two segments, the vertical derivatives are computed separately by two fourth order Lagrange interpolation polynomials in the forebody boundary layer and in the flow underneath the shroud.

With the present formulation, all the following physical phenomena have been taken into consideration: 1. the interaction between the inviscid flow and the viscous flow is defined by the free interaction Eqs. (13) and (14) along the external edge of the viscous layers; 2. the interaction between the shear layer and the recirculating core is accounted for by enforcing the continuity of the flow variables and their vertical derivatives $\partial/\partial\eta$ across the strip in segment 3; 3. the upstream propagation of pressure wave through the shear layer near the trailing edge of the shroud is implicitly included through the application of Navier–Stokes equations in the near wake region (segments 2 and 3) and the iterative numerical scheme; and 4. the existence of the base wall thermal boundary layer is explicitly formulated using the boundary layer equations along the base wall. If the validity of these equations is questioned near the upper left corner underneath the shroud in segment 1, because of the nature of the boundary conditions applied there, either the Navier–Stokes or the boundary layer equations would yield approximately the same results.

To employ the present scheme, we should remember that no singularity can be allowed in the domain of interest except right at the segment junction points where

the Poincaré analysis can be carried out in advance. From Eqs. (23) and (24) it is clear that the rear stagnation point is a singular point of the differential equations in segments 4 though 11. Since the location of the rear stagnation point is not known *a priori*, it poses a serious problem, because during the iteration this point may emerge in the integration domain such that the integral curves near it contain errors of an unacceptable magnitude. This difficulty can be avoided if the Lagrange interpolation polynomials are replaced by other forms of analytic functions; however the advantage of having the ordinary differential equations written in explicit form is lost. We will pursue only the solutions upstream of the rear stagnation point.

Boundary Conditions

Initial Thermal Boundary Layers

External to the shrouds, boundary conditions correspond to the solutions of forebody thermal boundary layers. Assuming no separation is ahead of the shroud trailing edge, the solutions of the compressible boundary layer past a flat plate are applied. With Prandtl number equal to unity, we have

$$\frac{T}{T_e} = 1 + \frac{\gamma + 1}{2} M_e^2 \left[1 - \left(\frac{u}{u_e}\right)^2\right] + \frac{T_w - T_{ad}}{T_e}\left(1 - \frac{u}{u_e}\right). \tag{27}$$

Near Wake Solutions

The downstream boundary condition is a near wake profile obtained by extrapolating Kubota's[1] far wake solution upstream. Defining $\bar{x}$, $\bar{y}$ as the coordinates after a Stewartson–Illingworth transformation and with the origin set at the neck, we have

$$\frac{u}{u_e} = 1 - \frac{A}{\sqrt{\bar{x}}} e^{-\bar{y}^2/4\bar{x}}$$

$$\frac{h}{h_e} = 1 + \frac{B}{\sqrt{\bar{x}}} e^{-Pr\bar{y}^2/4\bar{x}} \tag{28}$$

where

$$A = \frac{1}{2}\left(\frac{Re}{\pi}\right)^{1/2} \left(\frac{\rho_e u_e \theta}{\rho_\infty u_\infty H} M_e^2\right)_{\text{at neck}},$$

$$B = \frac{1}{2}\left(\frac{Re\, Pr}{\pi}\right)^{1/2} \left[St + \left(\frac{\rho_e u_e^3 \theta}{\rho_\infty u_\infty C_p T_{t\infty} H}\right)_{\text{at neck}}\right],$$

[1] Kubota, T.: Laminar Wake With Streamwise Pressure Gradient, GALCIT Hypersonic Research Project. Internal Memorandum No. 9, May 1962.

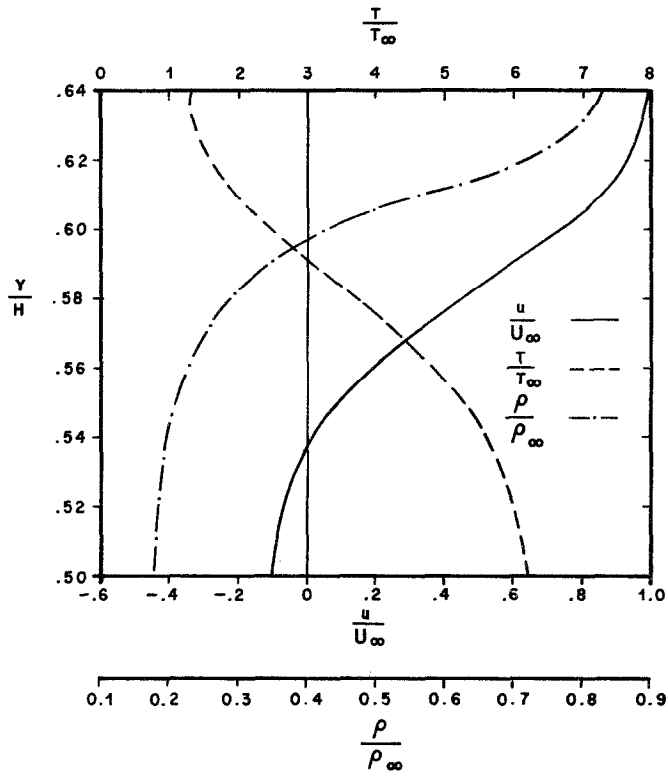

FIG. 4. Near wake boundary profiles.

and θ is the momentum thickness. Since the external flow is represented by the Prandtl-Meyer solution in the present study, the neck condition corresponds to that when the flow is parallel to the centerline. For the present problem, with $M_\infty = 11$, the $M_{e_{\text{at neck}}} = 9.586$. The total heat loss of the flow past the vehicle is estimated by neglecting the base heat transfer and assuming the vehicle length is 20 times the base height, so that the Stanton number is taken to be -0.0856155. The $(\theta/H)_{\text{at neck}}$ was put equal to 0.0618602 and $\Psi_*/H = 0.6389918$. Figure 4 shows the near wake profiles.

NUMERICAL PROCEDURES — MULTIPLE SHOOTING METHOD AND CONTINUATION METHOD

A serious shortcoming of the shooting method becomes apparent when the differential equations amplify the errors so rapidly that divergence occurs before the initial value problem can be completely integrated. This may happen even

though accurate guesses are made for the initial values. The multiple shooting method can frequently circumvent the difficulty, or else a finite difference scheme can be employed. The method is essentially a combination of difference scheme and initial value problems. It is designed to suppress the growth of the errors in the trial integral curves by dividing the domain of integration into a number of subintervals, integrating each individual initial value problem over its own interval, and then simultaneously adjusting all the guessed initial data to satisfy the boundary conditions and continuity conditions at the junction points.

The formulation of the multiple shooting method can be found in Osborne [6], and a comprehensive version was given by Bulirsch [4]. He also gave a detailed description of numerical computations of the Jacobian matrix and the application of Broyden's technique [7]; these will not be iterated here. The following brief discussion of the convergence of the shooting method given by Meng [8], however, will be included for completeness.

Let r and $\tilde{y}$ be the boundary conditions and the unknown vector; therefore, the convergence sphere and rate of convergence for the shooting method are

$$(1 - \sqrt{(1 - 2h_0)})\, \eta_0 h_0$$

and

$$(2h_0)^{2^{l-1}}\, \eta_0 / 2^{l-1},$$

with the Jacobian matrix G.

$$\| G \| \leqslant B_0 ,$$

$$\sum_{j,s=1}^{NS} \left\| \frac{\partial^2 r_i}{\partial \tilde{y}_j\, \partial \tilde{y}_s} \right\| \leqslant K$$

for all i's,

$$\| G^{-1} r \| \leqslant \eta_0 ,$$

$$\| r \| = \max_{1 \leqslant i \leqslant NS} | r | ,$$

$$\| G \| = \max_{1 \leqslant i \leqslant NS} \sum_{k=1}^{NS} | G_{ik} | ,$$

and l is the number of iterations counted after the initial values fall within the convergence sphere. By the Kantorovich theorem [9], the convergence is guaranteed as long as $h_0 = B_0 \eta_0 K$ is smaller or equal to one-half. For simple problems, convergence can often be obtained by simply going through many iterations. In complex problems, one has to modify the guessed values to fulfill as many of the Kantorovich sufficient conditions as possible for convergence. Ironically, the labor

required to make such a test is NS times more than that needed for solving the problem itself. For example, the quantity K needs integration of

$$MNS(N^2S^2 + 2NS - 1)/2$$

equations throughout the entire domain so that the advantage of working with the Cauchy-type problem will be greatly diminished. Since the Kantorovich h_0 cannot be obtained economically for the present problem, to illustrate how the multiple shooting method converges according to the theorem, we carried out a two-phase stagnation point flow solution. This was a smaller system of seven equations and four subintervals; the Euclidean error norm and h_0 are presented in Figure 5. One finds that the method does converge. Even the first guess falls outside the convergence sphere; as soon as it hits inside the sphere, the convergence is reached.

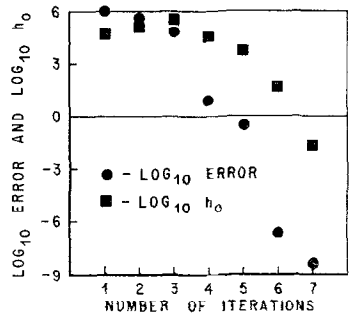

FIG. 5. Error norm and Kantorovich h_0.

The subdivision of the domain for the multiple shooting method is determined by the relation $| \xi_{j+1} - \xi_j | \sim 1/L_j$, if all the derivatives are Lipschitz continuous so that a stable integration can be guaranteed. In selecting this Lipschitz constant L_j, it is clear that the maximum row in the matrix G_j,

$$B_{0_j} = \max_{1 \leqslant i \leqslant N} \sum_{k=1}^{N} | G_{j_{ik}} | ,$$

is a measure of maximum local error growth resulting from small perturbations at the initial point of the subinterval j. Direct substitution of this value of B_{0_j} to determine the domain length, i.e., $\Delta\xi_j \sim 1/B_{0_j}$, however does not yield a practical answer for the multiple shooting method. Because the value of B_{0_j} is quite large in nonlinear problems, for example, it is of the order of 10^6 for the base wall boundary layer and of 10^3 for the downstream regions. Therefore in theory, about 10^3 or 10^6 subintervals to insure against the instability are required, but in practice the advantage of the Cauchy-type problem will be offset if the number of subintervals

becomes comparable to the number of the grids by the difference scheme. This dilemma can be resolved by incorporating the continuation method developed by Roberts and Shipman [10] with the multiple shooting method. They employed the simple shooting method and stretched the domain length to the final length in each iteration to solve a problem which could not be solved by the shooting method alone. It was shown [9] that the method will be stable if the stretched length is bounded by $1/2\bar{M}KB_{0_j}^2$; $\bar{M}$ is the uniform bound of the derivatives over $[\xi_j , \xi_{j+1}]_{\text{new}}$ and

$$K = \max_{1\leqslant i\leqslant N} \sum \left| \frac{\partial G_j}{\partial Y_{js}} \right| = \max_{1\leqslant i\leqslant N} \sum_{k,s=1}^{N} \left| \frac{\partial^2 \tilde{y}_i(\xi_{j+1})}{\partial Y_{js}\, \partial Y_{jk}} \right| .$$

However it is found that one should not continue the segment length this way in practice either because the denominator is very large, $\sim 0(10^{10})$, but should find the $\Delta\xi_{j\text{new}}$ by $\Delta\xi_{j\text{new}} = \Delta\xi_{j\text{old}}(\bar{M}KB_{0_j}^2)_{\text{old}}/\bar{M}KB_{0_j}^2)_{\text{new}}$, once one can have a stable integration over the $\Delta\xi_{\text{old}}$. By the present experience, $\Delta\xi_{j\text{new}} = \Delta\xi_{j\text{old}}B_{0_j\text{old}}^2/B_{0_j\text{new}}^2$ was found adequate in stretching the domain length during each iteration.

In summary by applying Broyden's correction technique, the convergence factor, and the continuation method to the multiple shooting method, the present problem was solved using 12 subintervals during the first few iterations. In following iterations closer to the convergence, the number of segments was reduced to eight without any effect upon the stability.

Finally it should be noted that the success of the present iteration scheme relies heavily upon the accuracy of the integration routine; a seventh order Runge–Kutta scheme with stepsize control established by Fehlberg [11] was hence applied in the present analysis.

Results and Discussion

The present problem is reduced to a system of 33 equations after applying the symmetry condition along the centerline and the interaction equation along the shear layer. The computation was conducted on a UNIVAC 1108 computer. The program occupies a 54K storage space. In initial trials six segments were employed, and the convergence appeared poor. Later double precision and 12 segments were used; this improved the convergence. The bulk of the computation time was spent in generating the Jacobian matrix, nearly 2.67 min each time; however by employing Broyden's technique, the time was reduced to 4.71 min to complete four iterations. The Jacobian matrix was first computed every five iterations with Broyden's technique applied accordingly; the solution yielded obvious errors. It appeared that the method produces the best result if the Jacobian matrix is computed every three iterations.

The Euclidean error norm $\sum_{j=1}^{M} | h_j |^2$ and the variation of the convergence factor (see Meng [8]) are shown in Fig. 6. The error decreases steadily for the first 13 iterations then oscillates, and the convergence factor shows similar features.

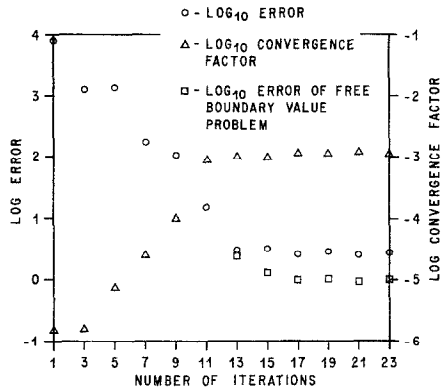

FIG. 6. Euclidean error norm and convergence factor versus iteration.

This lack of convergence was conjectured primarily because of fixing the segment lengths by the considerations of stability alone, as was outlined previously. Since each set of differential equations applied in different segments has its own physical capabilities or limitations to generate certain flow patterns, the associated segment lengths over which these equations are integrated would therefore play an important role in achieving convergence. Based upon this the first three segment lengths were then treated as additional unknowns; hence the system was augmented to 36 equations, and the problem was solved as a multiple free broundary-value problem. The convergence is improved (Fig. 6), although the oscillation still persists. The final segment configuration indicates that the base wall boundary layer thickness equals $0.07478H$, the two Navier–Stokes equation segments are of $0.014784H$ and $0.01118H$ respectively followed by eight boundary layer equation segments of $0.16H$ each. The segment lengths vary little with the free stream Reynolds number. The continuation method which was mentioned in the last section succeeded in stretching the whole domain length from $0.2H$ to $0.68H$ smoothly.

The evolution of the velocity vector and temperature contours through iterations to satisfy the boundary conditions and continuity across the subintervals are shown in Meng [8]; here we will present the final results only. Fig. 7a shows the shear layer is accelerated under the influence of the favorable pressure gradient before it reaches the edge of the shroud, and the velocities in the recirculating region have a maximum value of about 1 % of external flow velocity. The vertical dimension of the reverse flow region is small in the region $x/H > .3$. It is apparent that there are

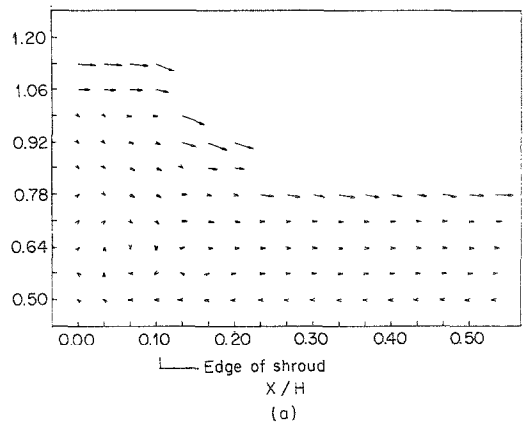

FIG. 7a. Velocity vector in the two-dimensional Space Shuttle base region. Free stream Mach no. = .1100 + 02; Reynolds number = .1000 + 06; free stream temperature = .3923 + 03; upper shroud edge mach no. = .1240 + 02; Prandtl number = .1000 + 01; base wall temperature = .4600 + 03; lower shroud edge mach no. = .1240 + 02; Angle of attack = .0000; and total temperature = .8500 + 04.

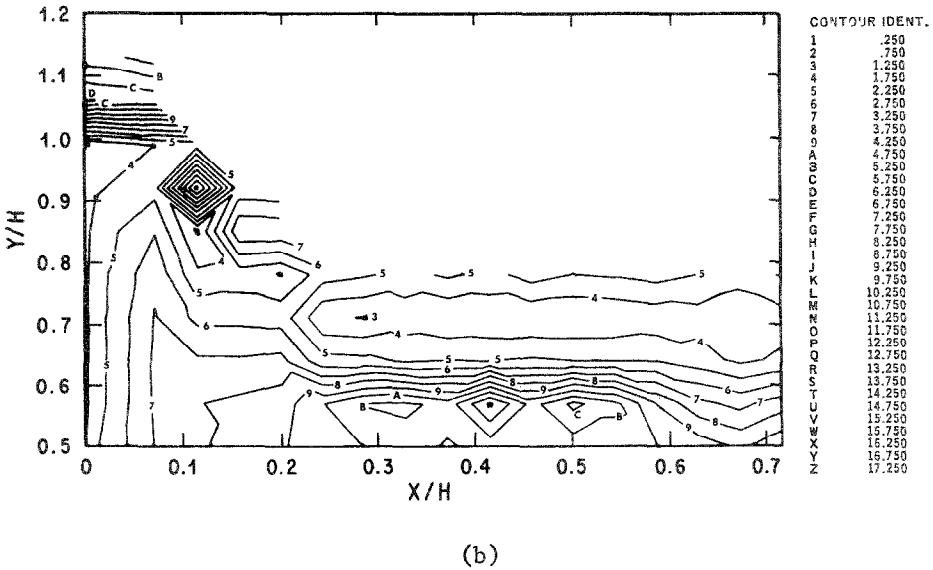

(b)

FIG. 7b. Temperature contour in the two-dimensional Space Shuttle base region.

still discontinuities in the velocity across the segments at $x/H = .1$ and .2. This error could not be reduced further with more iterations, its magnitude oscillates as depicted in Fig. 6 by the square symbols. The boundary conditions on the base wall ($x/H = 0$) and on the shroud ($y/H = 1$ and $x/H < .1$) are satisfied. It is interesting to find the horizontal velocity on the plane ($x/H = .1$) has two maxima, one is at $\eta = 1.13$ and another at $\eta = .78$. The velocity on the centerline is always horizontal and in the reverse direction; in fact, we are dealing with only the flow upstream of the rear stagnation point. The fact that the contour lines failed to be normal to the centerline in Fig. 7b indicates that errors resulting from the Lagrange interpolation exist. In an area near the wall, the gap between the contours is small because of the high heating rates. The cold and hot spots emerge in Figure 7b and the profiles show little variations along the horizontal direction throughout the near wake region. The diamond shape of the temperature contour in Figure 7b shows that some discontinuities exist across the segment even though the rest of the region shows quite results. From the temperature contour plots, it is clearly seen that

generated in the shear layer to the compression region and recirculates it back along the centerline. The effects of the protruding shrouds upon the base thermal environment would be to pull the pressure rise and high heat flux occurring in the recompression region away from the base wall so that the heating problems to the base wall and engines are reduced.

Since the plot routines pick up values only at equal vertical intervals, the flow variables on the shear layer edge are often missed in the temperature contours and velocity vector plots. The edge Mach number and pressure distributions are given

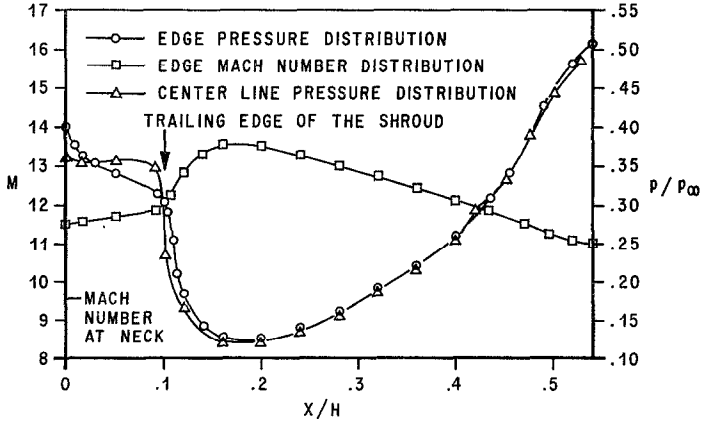

FIG. 8. Mach number and pressure distribution along the shear layer edge.

in Fig. 8 for Reynolds number $Re_{\infty,H} = 10^5$. The pressure first drops smoothly along the forebody boundary layer and then reaches the base pressure drastically near the trailing edge of the shroud, while the edge Mach number increases in the same manner. The pressure distribution on the centerline is also shown in Fig. 8; it is nearly constant throughout the cavity region until near $x/H = 0.1$ where it begins to follow the external pressure very closely. The Mach number at the neck, $\cong$9.587, is also marked in the same figure; if the external flow were parallel to the centerline. the external Mach number should be equal to this value. The vertical pressure distributions for $\mathrm{Re}_{\infty,H} = 1.2 \times 10^5$ at various axial locations are shown in Fig. 9. The pressure in the forebody boundary layer and downstream shear

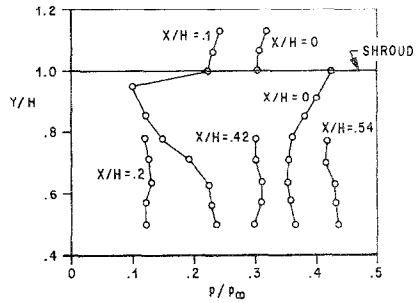

FIG. 9. Vertical pressure profiles at various axial locations.

layers is nearly constant except for interpolation errors; the pressure in the cavity on the base wall is nearly four times higher than that at the trailing edge. At $x/H = 0.1$, the pressure drops drastically underneath the shroud trailing edge and the value on the centerline is close to that on the external edge.

The heat transfer coefficients based upon the recovery temperature are shown in Fig. 10. The maximum heating rate is always on the centerline and its value increases monotonically with the free stream Reynolds number. Detailed flow patterns for various Reynolds number are given in Figs. 11, 12 and 13. From the velocity vector plots of Figs. 11a, 12a, and 13a, we can find that the shroud edge Mach numbers (shown on the top of the plot) varies slightly and monotonically with the free stream Reynolds numbers (also shown on the top of the figure) and the vector plots are quite similar although the convergence was even poorer for higher Reynolds numbers. Corresponding temperature contours for various cases are presented in Figs. 11b, 12b and 13b; the same dimensionless contour identification values T/T_∞ for all cases are listed on the right-hand side.

In Fig. 11b, the diamond shape discontinuity disappears for the lower Reynolds number case. The highest temperature values in the base region are indicated by the contour $E(T = 6.75T_\infty)$ in Fig. 11b near $x/H = .4$, by the contour $D(T = 6.25T_\infty)$

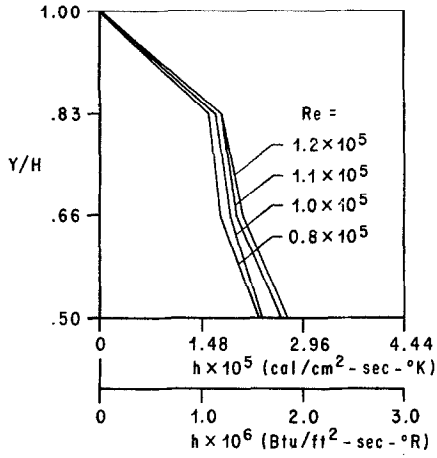

FIG. 10. Heat transfer coefficient on base wall versus Y/H_0.

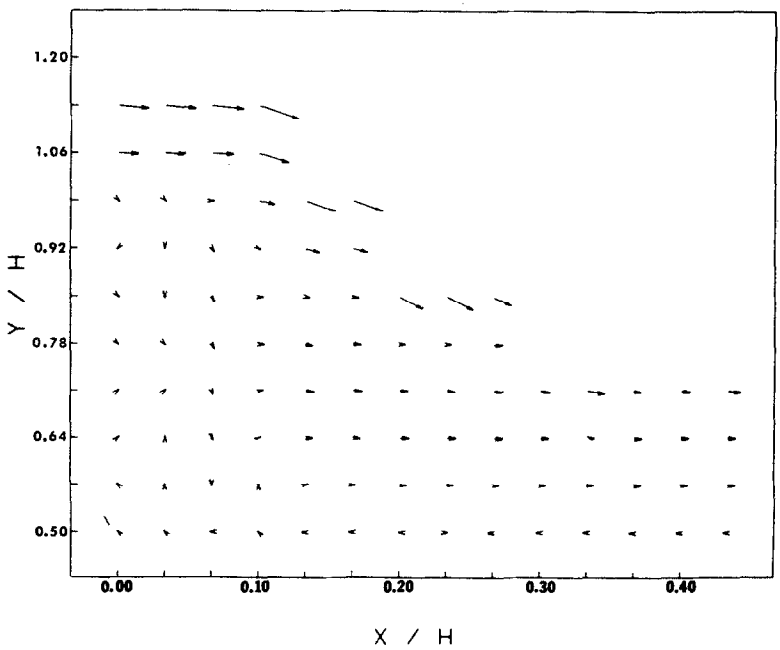

FIG. 11a. Velocity vector in the two-dimensional Space Shuttle base region for Re = 0.87×10^5. Free stream Mach no. = .1100 + 02; Reynolds number = .8700 + 05; free stream temperature = .3923 + 03; upper shroud edge Mach no. = .1237 + 02; Prandtl number = .1000 + 01; base wall temperature = .4600 + 03; lower shroud edge Mach no. = .1237 + 02; angle of attack = .0000; and total temperature = .8500 + 04.

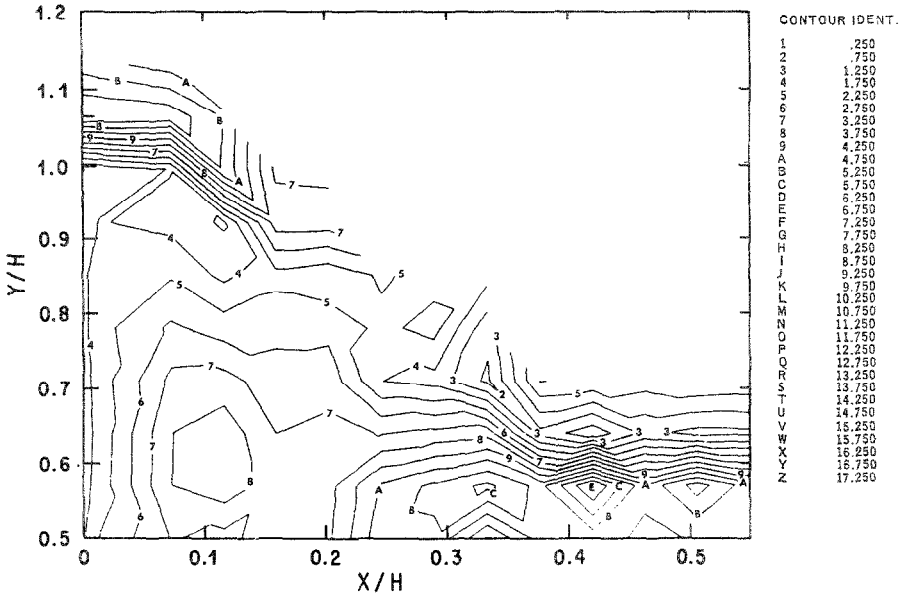

FIG. 11b. Temperature contour in the two-dimensional Space Shuttle base region for $Re = 0.87 \times 10^5$.

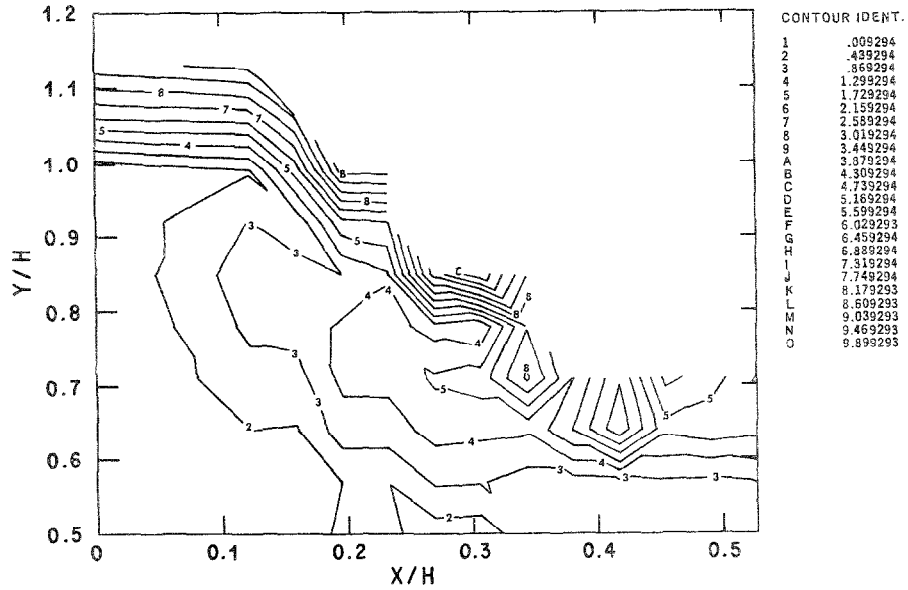

FIG. 11c. Mach number contour in the two-dimensional Space Shuttle base region for $Re = 0.87 \times 10^5$.

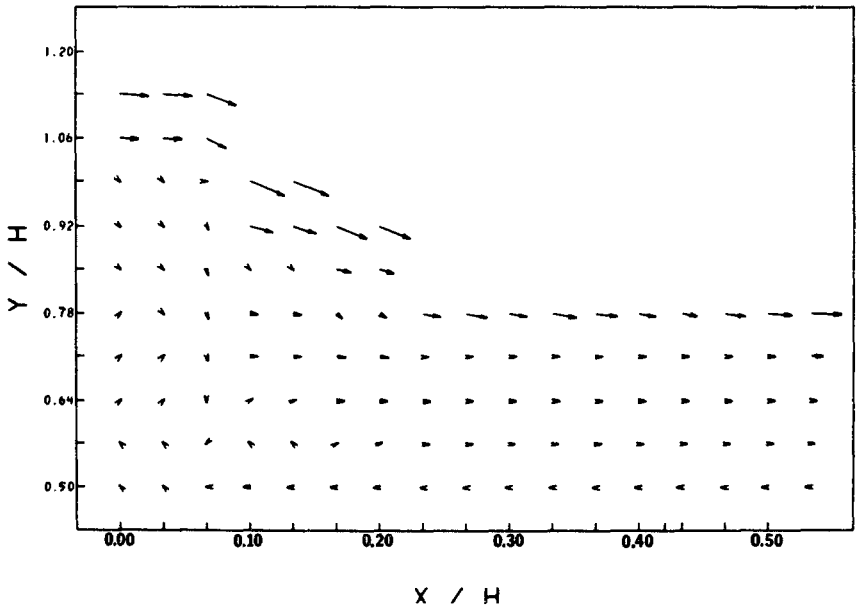

FIG. 12a. Velocity vector in the two-dimensional Space Shuttle base region for $Re = 1.1 \times 10^5$. Free stream mach no. = .1100 + 02; Reynolds number = .1100 + 06; free stream temperature = .3923 + 03; upper shroud edge mach no. = .1242 + 02; Prandtl number = .1000 + 01; base wall temperature = .4600 + 03; lower shroud edge mach no. = .1242 + 02; angle of attack = .0000; and total temperature = .8500 + 04.

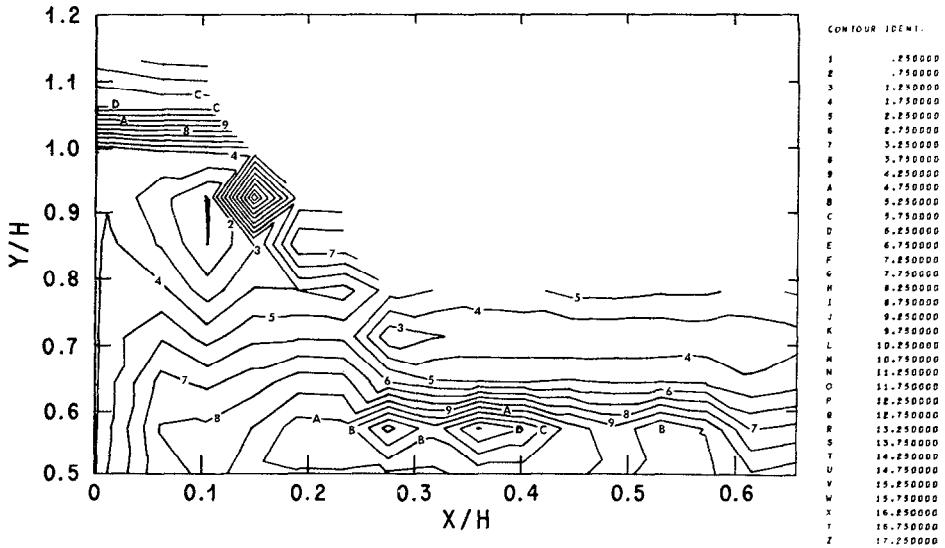

FIG. 12b. Temperature contour in the two-dimensional Space Shuttle base region for $Re = 1.1 \times 10^5$.

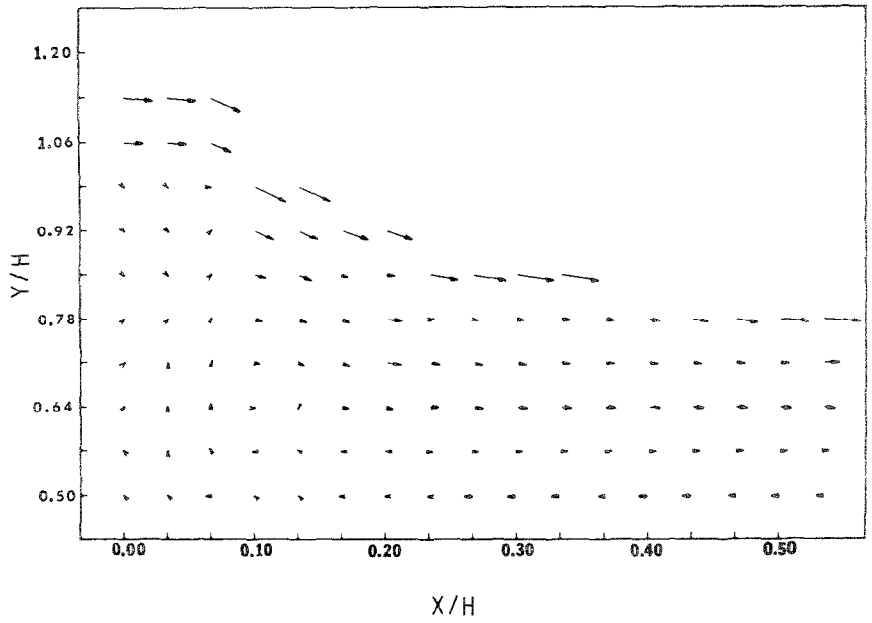

FIG. 13a. Velocity vector in the two-dimensional Space Shuttle base region for $Re = 1.2 \times 10^5$. Free stream Mach no. = .1100 + 02; Reynolds number = .1200 + 06; free stream temperature = .3023 + 03; upper shroud edge Mach no. = .1265 + 02; Prandtl number = .1000 + 01; base wall temperature = .4600 + 03; lower shroud edge Mach no. = .1265 + 02; angle of attack = .0000; total temperature = .8500 + 04.

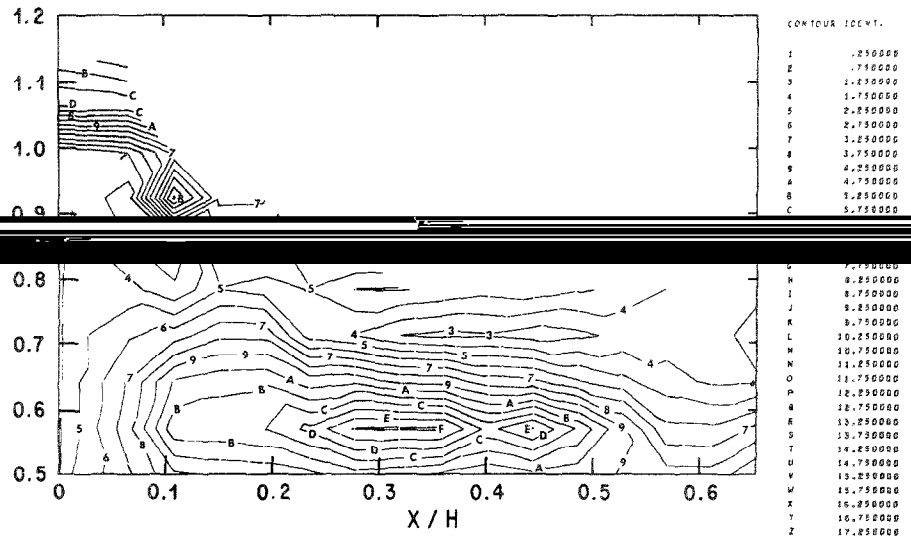

FIG. 13b. Temperature contour in the two-dimensional Space Shuttle base region for $Re = 1.2 \times 10^5$.

in Fig. 12b near $x/H = .35$. The hot spot is always located in the same area and is off the centerlines. It is not certain, however, that the hot spot will move toward the base wall when the free stream Reynolds number increases. The Mach number contour is also shown for the $Re_{\infty,H} = 0.87 \times 10^5$ case in Fig. 11c. The major portion of the recirculating core is subsonic, the sonic line extends from the wake into the forebody boundary layer, and external to it the viscous layer is entirely supersonic. The subsonic region in the forebody boundary layer is very thin so that little upstream influence can be transmitted through this viscous layer. This may explain the weak upstream influence observed in the experimental study of near wakes by Batt and Kubota [12]. The fact that a significant portion of the viscous layer is supersonic also confirms that the imbedded shocks will emerge deeply in the viscous region as was suggested by Weiss and Weinbaum [13].

Although we do not intend to dwell on the aspects of comparing the present results to experimental data since the latter do not exist for the present flow conditions and geometry, it is still interesting to compare the present results to those of Larson *et al.* [14]. They found $Nu \cong 100 \sim 150$ for $T_w = 0.34 \sim 0.716 T_{t\infty}$ at $M_\infty = 3$ and $Re_{\infty,H} \cong 10^7$, while the present study gives $Nu \cong 5$ for $T_w = 0.046$ $T_{t\infty}$ at $M_\infty = 11$ and $Re_{\infty,H} \cong 10^5$. The observed trend that the base wall thermal boundary layer thickness varies with both the Reynolds number and temperature difference between the wall and recirculation region is believed to be correct. Fig. 14 shows the value

$$\frac{Nu}{(Re)^{1/2}} = \frac{\beta T_\infty}{(T_{aw} - T_w)\left(\left(\frac{\rho u}{T}\right)_{\text{edge}} Re_{\infty,H}\right)^{1/2}}$$

obtained in comparison with the similar solution for a two-dimensional stagnation point flow solution given by Cohen and Reshotko [15]. The values scattered around the theoretical value ≈ 0.506, and they reveal no strong dependence upon the local

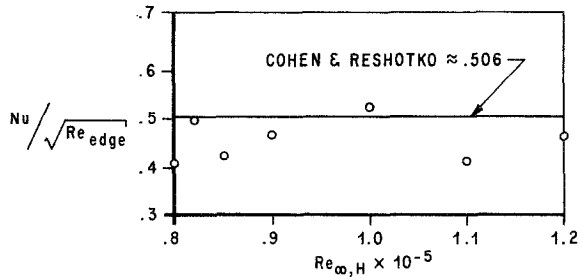

FIG. 14. Comparison with the two-dimensional stagnation point flow solution.

edge Reynolds number. The two-dimensional stagnation point flow is therefore seen as a close approximation of the base flow. Furthermore as shown by v/U_∞ versus y/H on the base wall boundary layer edge in Fig. 15, the magnitude of the vertical velocity decreases as the Reynolds number increases, and the linear dependence upon the coordinate y/H is true only near the centerline. For practical purposes, it can be asserted that the base flow is a stagnation point type flow; the maximum heating rate can be derived from the stagnation point flow results so long as the local Reynolds number can be estimated.

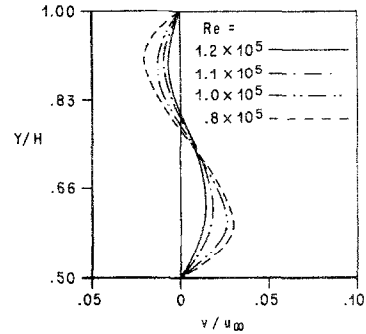

FIG. 15. Velocity (v) near the edge of the base wall boundary layer.

For future investigations of even higher Reynolds number flows by the present method, the following considerations should be noted. First the instabilities encounteres for integration across the base wall thermal boundary layer can be avoided if a variable transformed coordinate is incorporated to allow different stretching in various segments. Secondly it should again be emphasized that when using Lagrange interpolation polynomials in formulating a Cauchy problem, there should exist no singularity in the flow domain, because when such singularity emerges, the advantage of using the Lagrange interpolation polynomials will be lost. Replacing the Lagrange interpolation polynomials by other sets of polynomials or analytic functions can remove this singularity, but one more matrix inversion to obtain the system of first order differential equations would then be necessary. To include the solution downstream of the rear stagnation point, such replacement is needed.

Although for simplicity we have concentrated on the zero angle of attack case, extensions to skew cases offer no difficulty. The various aspects of the rate of convergence, the storage requirement, the computation time, and the exactness of the solution on the strips favor the present method when it is compared to many existing schemes which deal with high Reynolds number flows, provided the flow has a finite domain and contains no singularity.

REFERENCES

1. G. F. TELENIN AND G. P. TINYAKOV, A method for computing the three-dimensional flow around bodies, accompanied by a detached shock wave (Metod rascheta prostranstvennogo obtekaniya tel s otoshedshey udarnoy volnoy), *Doklady AN SSR* **154**, No. 5, (1964).
2. MAURICE HOLT AND E. NDEFO, A numerical method for calculating steady unsymmetrical supersonic flow past cones, *J. Comp. Phys.* **5** (1970), 463–486.
3. D. D. MORRISON, J. D. RILEY, AND J. F. ZANCANARO, Multiple shooting method for two-point boundary value problems, *Comm. ACM* **5** (1962), 613–614.
4. R. BULIRSCH, "Einführung in die Numerische Mathematik II," Heidelberger Taschenbuch 114, Springer, N.Y., 1973.
5. S. M. GILINSKIY, G. F. TELENIN, AND G. P. TINYAKOV, A method for computing supersonic flow around blunt bodies, accompanied by a detached shock wave, NASA TT F-297, February 1965.
6. M. R. OSBORNE, On shooting methods for boundary value problems. *J. Math. Anal. Applic.* **27** (1969), 417–433.
7. C. G. BROYDEN, A Class of Methods for Solving Nonlinear Simultaneous Equations. *Math. Comp.* **19** (1965), 577–593.
8. J. C. S. MENG, A new technique for calculating reentry base heating, NASA TN D-7508, Dec. 1973.
9. S. M. ROBERTS AND J. S. SHIPMAN, Two-point boundary value problems: shooting method *in* "Modern Analytic and Computational Methods in Science and Mathematics," (Richard Bellman, Ed.), Vol. 31, Elsevier, 1971.
10. S. M. ROBERTS AND J. S. SHIPMAN, Continuation in shooting methods for two-point boundary value problems, *J. Math. Anal. Applic.* **18** (1967), 45–58.
11. E. FEHLBERG, Classical fifth-, sixth-, seventh-, and eighth-order Runge–Kutta formulas with stepsize control, NASA TR R-287, October 1968.
12. R. G. BATT AND T. KUBOTA, Experimental investigation of laminar near wakes behind 20° wedges at $M_\infty = 6$, *AIAA J.* **6** (1968), 2077–2083.
13. R. WEISS AND S. WEINBAUM, Hypersonic boundary layer separation and the base flow problem. *AIAA J.* **4** (1966), 1321–1330.
14. R. E. LARSON, A. R. HANSON, F. R. KRAUSE, AND W. K. DAHM, Heat transfer below reattaching turbulent flows, AIAA Paper No. 65-825, December 1965.
15. C. B. COHEN AND E. RESHOTKO, The compressible laminar boundary layer with heat transfer and arbitrary pressure gradient, NACA Report 1294, February 1955.